# Supporting Information

## Pertsinidis et al. 10.1073/pnas.1310654110

### SI Methods

**Microscope Setup.** The setup was built around an inverted optical microscope (Olympus IX-71) with an oil immersion (Nikon 60× N.A. = 1.49) objective lens. For fluorescence excitation we used an ~640-nm diode laser (Opnext) and a 532-nm solid-state laser (Melles-Griot), coupled into a single-mode optical fiber. For the separate focus-lock laser system we used a fiber-coupled 785-nm NIR diode pigtail (Thorlabs; LPS-PM785-FC). The diode was driven by a precision current source (Thorlabs; LDC201CU) and its temperature regulated with a thermoelectric cooler (Thorlabs; TED200C) to achieve stable emission.

In this implementation special care has to be exercised to ensure that the two separate detection systems (feedback stabilization CCD1 and superresolution imaging CCD2) remain registered during the data acquisition, e.g., as demonstrated with active optics for two-color imaging (1). In practice, we successfully used an open-loop feedback by relying on tight regulation of the room temperature ($\Delta T_{\text{p-p}} < 0.5\ °C$) to passively maintain registration between the two detectors at <3 nm peak-to-peak over 1 h (Fig. S1). If present during prolonged acquisitions, the ~1- to 2-nm residual drift in the data can be corrected in post-processing.

To achieve passive stability of the apparatus, we tuned the building temperature control feedback loop, regulating the temperature of the air entering the room with a reheat coil, to achieve less than 0.5 °C peak-to-peak variation over 1 d, using knowledge of feedback systems gained during the development of the microscope feedback controls. In addition, enclosing the microscope and all associated optical components further dampened fast temperature fluctuations (to <0.1 °C on the timescale of ~1 h) as well as mechanical disturbances from air currents.

The laser beams were combined using dichroic mirrors (Chroma) and delivered to the microscope with a polychroic mirror (Chroma) that reflected all laser beams but allowed transmission of emitted fluorescence. Either a blue (Thorlabs; M455L1, 455-nm emission peak) or a white light-emitting diode (Thorlabs; MCWHL1) facilitated simultaneous bright-field fluorescence imaging. The image on the side port of the microscope was split with a long-pass dichroic (Omega; 505DCLP) and the blue light was projected with relay lenses on a fast CCD (Andor; DV860DCS-BV, CCD1). The fluorescence image was further magnified, split by a long-pass dichroic with extended reflection (Chroma; 645DCXR), band-pass filtered to select cyanine-3 (Cy3) or Cy5 emission (Chroma; HQ570/50, HQ700/100), and projected onto two regions of the CCD (Andor; DV897CSO-BV, CCD2).

We note that real-time tracking of fiducials like luminescent gold nanoparticles or fluorescent microspheres imaged directly on CCD2 used for the single-molecule detection can also be used for feedback stabilization (Fig. S1I), significantly simplifying the instrument design, with the additional advantage that the feedback loop and the single-molecule localizations are inherently registered. The advantage of a separate position feedback system is higher loop bandwidth and thus higher stability, as well as the flexibility of separately optimizing the servo-loop and the fluorescence imaging parameters. Furthermore, by stabilizing the microscope and imaging all nearby molecules on the same CCD regions one can minimize the effect of CCD nonuniformity.

**Single-Molecule Tracking.** In each CCD frame, a 13 × 13 (pixels)$^2$ region of interest (ROI) centered around each molecule was

fitted to a 2D Gaussian function to identify the center coordinates $\{x, y\}$, the width of the Point Spread Function in two orthogonal directions $\{s_x, s_y\}$, the peak height $A_0$, and background level $B$. Spots tracked over consecutive frames that appeared centered within a radius of 1 pixel were regarded as the same molecule and assigned the average values of $\{x, y\}$, $\{s_x, s_y\}$, $A_0$, and $B$ over all of the frames.

We estimated the number of photons $N$ collected from each molecule per switching cycle by the total counts over the 13 × 13 ROI (from all frames in that molecule's stack, after background subtraction). Alternatively (for Fig. 2C only), we estimated $N$ from the 2D Gaussian fit as $n = 2\pi s^2 A_0$, where $s = \sqrt{s_x s_y}$. The precision $\sigma$ in the coordinates for each molecule was calculated on the basis of Eq. **S1a**, using an effective background term $n_{\text{frames}} b^2$ for a molecule tracked over $n_{\text{frames}}$ total frames and including a contribution of $b_0^2 = (5.2)^2$ photons$^2$/pixel from the CCD read-out electronic noise. Histograms for $N$ and $\sigma$ are shown in Fig. S2.

**Derivation of the Photon-Noise–Limited Superresolved Point-Spread Function.** Fluorescence photons encode information about the position of the emission source, with a single photon providing a spatial uncertainty of order the wavelength $\lambda$ (2). For fluorescence photons collected through the aperture of a microscope objective lens and imaged on a pixelated detector, with pixel size $a$ (in units of nanometers) and background rms noise in each pixel $b$ (number of photon counts), the statistical uncertainty $\sigma$ in the position of the fluorescence emitter is (3)

$$\sigma^2 = \frac{s^2 + a^2/12}{N} + \frac{8\pi\, s^4}{a^2}\frac{b^2}{N^2}, \qquad \textbf{[S1a]}$$

where $s$ (in nanometers) is the SD of the image point-spread function and $N$ is the total number of collected photons. The pixelation noise assumes a top-hat distribution of size $a$ and is valid when $s > a$ (3). We note that a more theoretical accurate treatment yields (4)

$$\sigma^2 = \frac{16}{9}\frac{s^2 + a^2/12}{N} + \frac{8\pi\left(s^2 + a^2/12\right)^2}{a^2}\frac{b^2}{N^2}. \qquad \textbf{[S1b]}$$

For our experimental conditions the predictions of Eqs. **S1a** and **S1b** differ by <15% (Table S1).

In each on cycle, each dye molecule emits an exponentially distributed number of collected photons $N$,

$$D(N) = \frac{1}{N_0} e^{-\frac{N}{N_0}}, \qquad \textbf{[S2]}$$

where $N_0$ is the mean number of collected photons. The distribution of the position uncertainty $\sigma$ in each cycle is $D(\sigma)d\sigma = -D(N)dN \Rightarrow D(\sigma) = -D(N)\frac{dN}{d\sigma}$; thus assuming for simplicity no background and pixelation noise,

$$\frac{dN}{d\sigma} = -\frac{2s^2}{\sigma^3} = -\frac{2N}{\sigma} \ \text{ and } \ D(\sigma) = \frac{2\sigma_0^2}{\sigma^3} e^{-\frac{\sigma_0^2}{\sigma^2}}, \qquad \textbf{[S3]}$$

where $\sigma_0 \equiv \frac{s}{\sqrt{N_0}}$.

The distribution of the measured $x$ positions takes the form

$$D(x) \propto \int_0^{+\infty} e^{-\frac{x^2}{2\sigma^2}} D(\sigma)d\sigma = \int_0^{+\infty} e^{-\frac{x^2}{2\sigma^2}} \left(\frac{2\sigma_0^2}{\sigma^3}\right) e^{-\frac{\sigma_0^2}{\sigma^2}} d\sigma =$$

$$-\sigma_0^2 \int_{+\infty}^0 e^{-\frac{x^2+2\sigma_0^2}{2}\left(\frac{1}{\sigma^2}\right)} d\left(\frac{1}{\sigma^2}\right) = \frac{-2\sigma_0^2}{x^2+2\sigma_0^2} e^{-\frac{x^2+2\sigma_0^2}{2\sigma^2}}\Big|_{\sigma=0}^{\sigma=\infty}$$

and thus $D(x)$ has a Lorentzian peak shape

$$D(x) \propto \frac{2\sigma_0^2}{x^2+2\sigma_0^2}, \qquad \textbf{[S4]}$$

with full width at half maximum (FWHM) equal to $2\sqrt{2}\sigma_0 \approx 2.828\sigma_0$.

### Mathematical Basis for Resolution Enhancement by Statistical Refinement of Localization Data.
By enforcing a cutoff $\sigma_{cutoff}$ in the precision, the distribution of $x$ positions becomes

$$D(x) \propto \frac{2\sigma_0^2}{x^2+2\sigma_0^2} e^{-\frac{x^2+2\sigma_0^2}{2\sigma^2}}\Big|_{\sigma=0}^{\sigma=\sigma_{cutoff}} \propto \frac{2\sigma_0^2}{x^2+2\sigma_0^2} e^{-\frac{x^2}{2\sigma_{cutoff}^2}}, \qquad \textbf{[S5]}$$

the product of a Lorentzian with FWHM equal to $2\sqrt{2}\sigma_0 \approx 2.828\sigma_0$ and a Gaussian with FWHM equal to $2\sqrt{2\ln 2}\sigma_{cutoff} \approx 2.35\sigma_{cutoff}$. The FWHM can be expressed as

$$\gamma(\nu) \equiv FWHM(D)/\sigma_{cutoff} = 2\sqrt{2W\left(2\nu^2 e^{\nu^2}\right) - 2\nu^2}, \qquad \textbf{[S6]}$$

where the Lambert $W$ function is defined as $W(z)e^{W(z)} = z$ and the cutoff ratio $\nu$ is defined as $\nu \equiv \frac{\sigma_0}{\sigma_{cutoff}}$. The refinement process when $\sigma_{cutoff} < \sigma_0$ results in final FWHM resolution of roughly $2\sigma_{cutoff}$ [$\gamma(\nu) \to 2.355$ for $\nu \gg 1$, Fig. S3].

The ratio of the refined FWHM resolution over $\sigma_0$, $\beta(\nu) \equiv FWHM(D)/\sigma_0 = \gamma(\nu)/\nu$, decreases when a smaller $\sigma_{cutoff}$ is chosen (Fig. S3). Meanwhile, the fraction $\alpha$ of localizations kept,

$$\alpha \equiv \int_0^{\sigma_{cutoff}} D(\sigma)d\sigma = \int_0^{\sigma_{cutoff}} \frac{2\sigma_0^2}{\sigma^3} e^{-\frac{\sigma_0^2}{\sigma^2}} d\sigma = e^{-\nu^2}, \qquad \textbf{[S7]}$$

vanishes rapidly with increasing $\nu$ (Fig. S3). Thus, for a practical limit of $\alpha \sim 0.01 - 0.1$, two- to threefold resolution enhancement over the initial Lorentzian FWHM of $2\sqrt{2}\sigma_0 \approx 2.828\sigma_0$ can be achieved (Fig. S3).

### DNA Construct Preparation.
Modified DNA oligonucleotides (5′-Cy3-TTCGGGCAGCCTGCGGGGGA-Cy5-3′, 5′-biotin-AAAAAAAAAAACGGATCCCCCGCAGGCTGCCCGAATTC-CGG-3′) were synthesized and HPLC purified by Integrated DNA Technologies. To prepare duplexes we annealed the two complementary strands at 2 μM in 20 mM Tris·HCl (pH 7.9), 50 mM NaCl buffer at 95 °C for ~15 min followed by cooling to room temperature over ~2–3 h. Note that the presence of Cy3 at one end of the ~7-nm-long DNA duplex does not affect Cy5 photoswitching at the other end.

### Modified Microspheres.
Biotin-PEG (NEKTAR; Biotin-PEG-mSBA, 5 kDa) was grafted at 10% wt/vol to 0.5-μm diameter aliphatic amine polystyrene spheres (IDC) in a 0.1-M sodium bicarbonate solution (pH ~ 9). After PEGylation, the beads were washed and stored in PBS at 4 °C.

### F-actin Polymerization.
G-actin (1:12 biotininylated G-actin; Cytoskeleton Inc.) was diluted to 0.4 mg/mL in 5 mM Tris·HCl (pH 8.0), 0.2 mM CaCl$_2$, 1 mM DTT, and 0.2 mM adenosine triphosphate (ATP). F-actin polymerization was initiated by addition of 6 μL of 500 mM KCl/20 mM MgCl$_2$ and 5 μL of 100 mM ATP to 50 μL G-actin solution. After incubation at room temperature for ~2–3 h, 0.5 μL of 200 μM Alexa 647-Phalloidin (Invitrogen) was added and the formed filaments were stored at 4 °C until use.

### Sample Cells.
Grafting of "cloudy-point" PEG on glass slides and coverslips, assembly into sandwich sample cells, and attachment of biotinylated beads and Cy5 duplexes were prepared as described in ref. 1. For F-actin attachment, after incubation of the PEG-biotin surface with streptavidin, formed actin filaments were diluted 1:100 in 1× PBS (pH 7.4)/1 mM MgCl$_2$/0.2 mM ATP and bound to the surface for 5 min.

### Imaging Buffer.
For Cy5-DNA and SNAP-25 Alexa 647-immunostaining experiments, the oxygen-scavenging imaging buffer was 100 mM Hepes-KOH (pH 7.5), 160 mM KCl, 0.9% wt/vol glucose, 144 mM β-ME (Sigma), 1× glucose-oxidase/catalase enzyme stock[15], and 0.2% wt/vol BSA. β-ME appears to be stable under these conditions throughout the experiment (a few hours) as evidenced by efficient switching of the dyes. The composition of the imaging buffer was essential for achieving stable, oxygen-free conditions in the sample cell and efficient Cy5/Alexa 647 photoswitching. For the F-actin A647-phalloidin experiments the imaging buffer contained additionally 2 mM MgCl$_2$ and 0.2 mM ATP.

### Wild-Type Primary Mouse Neuronal Cultures.
Animal protocols used in this study, as well as the overall mouse husbandry practices, were approved by the Institutional Animal Care and Use Committee at Stanford University. Cortices from newborn mouse pups were dissected in ice-cold Hank's Balanced Salt Solution (HBSS), dissociated by trypsinization (0.05% trypsin-EDTA, for 10 min at 37 °C), triturated with a siliconized pipette in plating medium [MEM (Gibco) supplemented with 5 g/L glucose, 0.2 g/L NaHCO$_3$ (Sigma), 0.1 g/L transferrin (Calbiochem), 0.25 g/L insulin (Sigma), 0.3 g/L L-glutamine (Gibco), and 10% (vol/vol) FBS]. Dissociated cells were plated (100 μL) onto 12-mm coverslips, which were coated for ≥30 min with Matrigel at 37 °C (BD Biosciences). Plating medium was replaced with growth medium [MEM (Gibco) containing 5 g/L glucose, 0.2 g/L NaHCO$_3$ (Sigma), 0.1 g/L transferrin (Calbiochem), 0.3 g/L L-glutamine (Gibco), 5% FBS, 2% B-27 supplement (Gibco), and 2 μM cytosine arabinoside (Sigma)] 24–48 h after plating. Neuronal cultures were used for immunofluorescence or immune-blotting/-precipitation experiments at 14 d in vitro.

### Syntaxin-1A KO Neuronal Cultures.
Hippocampal neurons were cultured from neonatal syntaxin-1A KO mice, infected at 5–7 d in vitro (DIV5–7) with various lentiviruses, and analyzed at DIV13–16 essentially as described in ref. 5. Briefly, the mouse hippocampus was dissociated by papain digestion and plated on Matrigel-coated glass coverslips, and neurons were cultured for 13–16 d in MEM (Gibco) supplemented with B27 (Gibco), glucose, transferrin, FBS, and Ara-C (Sigma).

### Plasmid Construction and Production of Lentiviruses.
The packaging of lentiviruses and the infection of neurons with lentiviruses have been described in ref. 6. Briefly, the lentiviral expression vector and three helper plasmids, the pRSV-REV [plasmid expressing Human Immunodeficiency Virus 1 (HIV1) REV (Regulator of Expression of Virion Proteins) protein under control of the Rous sarcoma virus (RSV) U3 promoter], pMDLg/pRRE [packaging plasmid that includes the *gag* (group-specific antigen) and *pol*

(polymerase) HIV1 genes and an RRE (REV Response Element)], and vesicular stomatitis virus G protein (VSVG) were cotransfected into human embryonic kidney (HEK) 293T cells (ATCC) at 6, 2, 2, and 2 μg of DNA per 25-cm² culture area, respectively. The transient transfections were performed with FuGENE 6 transfection reagent (Roche) following the manufacturer's instructions. Supernatant with viruses was collected 48 h after transfection. Cortical neuronal cultures were infected at 5 DIV and used for biochemical or physiological analysis at 14–16 DIV. All steps were performed under level II biosafety conditions.

**Development and Validation of Syntaxin-1 shRNAs.** Syntaxin-1A and -1B cDNA sequences were aligned and two conserved regions were chosen as targets of shRNAs. The sequences of the two regions are AGA GGC AGC TGG AGA TCA C and GAT CAT CAT TTG CTG TGT G. The shRNA oligos were synthesized (the sense strands of the oligos were TCG ACC AGA GGC AGC TGG AGA TCA CTT CAA GA GAG TGA TCT CCA GCT GCC TCT GGT TTT TTG GAA AT, and CGC GCC CGA TCA TCA TTT GCT GT G TGT TCA AGA GAC ACA CAG CAA ATG ATG ATC ATT TTT TTG GAA A), annealed, and inserted into L309, using XhoI-XbaI and AscI and RsrII sites, respectively (6). The two shRNAs were driven by human H1 and U6 promoters, respectively. The effects of the syntaxin-1A and -1B were validated in wild-type cortical neuronal culture by Western blotting and quantitative RT-PCR. From Western blotting analysis we found that the shRNAs were more effective on syntaxin-1B than on syntaxin-1A, and thus we decided to do functional analysis on a syntaxin-1A knockout background to maximize the level of syntaxin-1 deficiency.

**Antibodies.** Monoclonal antibodies against SNAP-25 (SMI-81; Sternberger Monoclonals) and syntaxin-1 (HPC-1; Synaptic Systems), as well as secondary anti-mouse and anti-rabbit (Invitrogen), were labeled with Alexa 647-NHS (Invitrogen) or Atto 532-NHS (ATTOTEC) amine-reactive dyes in a 0.1-M $Na_2HCO_3$ solution (pH ∼ 9) for 30 min at room temperature. Unreacted dye was removed by five to six washes with PBS, using a Microcon concentrator (30-kDa cutoff; Millipore). Rabbit polyclonal antibody against mammalian uncoordinated-18 (Munc18-1) (P592) (7) was used unconjugated.

**Immunofluorescence Experiments.** Cultured neurons were washed (three times) with PBS and fixed for 20 min at room temperature in PBS/4% paraformaldehyde (PFA). Following three washes with PBS, the fixed cultures were permeabilized for 15 min in blocking solution [PBS/3% BSA (Sigma)/0.1% Triton X-100 (Sigma)]. Permeabilized neuronal cultures were incubated with conjugated, dye-labeled primary antibodies for 1 h in blocking solution at room temperature. Alternatively, 1 h incubation with unlabeled primary antibodies was followed by 1 h incubation with dye-labeled secondary antibodies. The coverslips postfixed in 4% PFA were rinsed (six times) with PBS and stored at 4 °C. Laser scanning confocal microscopy at diffraction-limited resolution (Leica TCS SP-2) was performed on coverslips mounted in Vectashied (Vector Labs). Titration of the primary antibody concentration determined staining conditions at which the available SNAP-25 and syntaxin-1 epitopes are saturated and confirmed axon-specific staining (Fig. S4). Experiments were performed close to saturation to ensure efficient staining.

**Immunoblotting and Immunoprecipitations.** Either brain homogenates or cultured neurons were solubilized in 50 mM Tris·Cl buffer (pH 7.4) containing 150 mM NaCl and 0.1% Triton X-100. Following centrifugation at $16,000 \times g_{av}$ for 10 min at 4 °C, the clarified lysate was used for immunoblotting (after addition of 2× SDS sample buffer containing 10% β-mercaptoethanol) or

subjected to immunoprecipitation. Immunoprecipitation was performed with the indicated primary antibodies and 30 μL of a 50% slurry of protein-G Sepharose beads (Amersham) for monoclonal IgG or protein-A Sepharose beads (GE Healthcare) for polyclonal rabbit sera, for 2 h at 4 °C. Control immunoprecipitations were performed with brain lysates with no antibody (for monoclonal antibodies) or with preimmune serum (for polyclonal rabbit sera). Following five washes with 1 mL of the extraction buffer, bound proteins were eluted with 2× SDS sample buffer containing 10% β-mercaptoethanol and boiled for 15 min at 100 °C. Coprecipitated proteins were separated by SDS/PAGE, with 5–10% of the input in the indicated lane.

**Electron-Beam Lithography of Calibration Arrays.** An ∼1,000-Å Al film was deposited on quartz wafers, followed by spin-coating an ∼2,500-Å layer of e-beam resist (ZEP-520). The nanohole array was written using a Raith-150 e-beam lithography tool as single-shot dots. The resist was developed in Xylene, followed by Methylisobutylketone:Isopropyl-alcohol (MIBK:IPA 1:3), with a final IPA rinse and blow drying. The hole pattern was transferred to the Al film, using reactive-ion etching (p5000; Applied Materials). Characterization was done with a scanning-electron microscope (Hitachi). The final hole diameter depended on the dose during e-beam exposure and varied between ∼90 nm and 250 nm.

**Two-Color Mapping Transformations.** We imaged the nanohole pattern simultaneously in the green and red channels of the CCD array (Fig. S6), obtaining a set of data $\{x_G^i\}$, $\{x_R^i\}$ composed of the apparent coordinates of each nanohole $i$, $x = (x, y)$ (Fig. S6). Translating the sample with the piezoelectric nanopositioning stage enabled us to sample the CCD array with finer resolution than the pitch of the hole pattern. We used two approaches to calibrate mapping transformations between coordinates in the green and red color images. In the simplest implementation we performed polynomial warping of degree $N$, to obtain matrices $P$, $Q$ that can be used to obtain the transformed coordinates [e.g., from red (R) to green (G)]:

$$x_{RG} = \sum_{k,l=0}^{N} P_{kl} x_R^k y_R^l, \qquad y_{RG} = \sum_{k,l=0}^{N} Q_{kl} x_R^k y_R^l. \qquad \textbf{[S8]}$$

We found that the typical registration accuracies achieved (Fig. S6) with such "global" transformations could not be significantly improved beyond ∼8 nm by increasing the order of the polynomial or by increasing the spatial sampling frequency. Previously we had shown that the photoresponse nonuniformity of the CCD array gives rise to high-spatial-frequency "noise" in such mapping transformations (1). Because the CCD array can be sampled very finely (down to subpixel level, ref. 1), a "local" approach that calibrates the mapping by spline interpolation can be used to achieve higher accuracy. According to this scheme, any point in, e.g., the red color, $\vec{x}_R$ can be mapped to a point $\vec{x}_{RG}$ in the green color by

$$\vec{x}_{RG} = \sum_{i=0}^{N_{pts}} c_i \phi\left(\left|\vec{x}_R^i - \vec{x}_R\right|\right) + c_0 + c_1 \vec{x}_R, \qquad \textbf{[S9]}$$

with $\phi(r)$ being an appropriately chosen radial basis function (8), centered on each calibration point $i$. Thin-plate splines ($\phi(r) = r^2 \ln(r)$) have been used in the past for image warping and registration. In practice we find that various choices of radial basis function, including thin-plate splines or multiquadratic interpolation [$\phi(r) = \sqrt{1 + (\varepsilon r)^2}$, with $\varepsilon$ the tunable parameter], give similar results. The coefficients $c_i$ are estimated by least-squares minimization and a regularization parameter (8, 9) $\lambda$ is

introduced to take into account the localization errors by weakening the interpolation conditions. For $\lambda = 0$, we obtain a perfect interpolation through the experimental points, whereas for increasing $\lambda$ the resulting mapping transformation is smoother. The limit $\lambda \to \infty$ corresponds to a first-order linear mapping. The most accurate transformation is thus obtained by optimizing the level of smoothing to filter out noise in the calibration data, without losing information on the underlying pattern of spatial distortions (Fig. S6).

To validate the mapping transformation obtained using spline interpolation, we imaged Cy3 and Cy5 attached to 20-bp dsDNA duplexes (1). Several areas of the coverslip were imaged to obtain up to 100 pairs of Cy3-Cy5 positions that were randomly dispersed over the whole field of view of the CCD. The registration accuracy obtained for Cy3-Cy5 using the spline interpolation algorithm was ~3 nm (Fig. S6). We note that the set of coordinates from Cy3 and Cy5 on the dsDNA molecules can also be used to directly calibrate the mapping transformations, providing additional experimental flexibility.

**Density-Based Analysis of Clustering Structure.** To analyze the structure of the clustering patterns of SNAP-25 and syntaxin-1 molecules we used the OPTICS algorithm, to perform a hierarchical ordering of the SNAP-25 or syntaxin-1 localizations. We also calculated suitable "core distances" $\{cdist^i_{GR}, cdist^i_{GG}\}$ for each, e.g., green localization point $i$, indicating the radius of an area centered on point $i$ that encompasses exactly $Minpts$ points (minimum number of points required forming a cluster) of the same or opposite color (Fig. S5). Thus, $\{cdist^i_{GR}, cdist^i_{GG}\}$ indicate the spatial extent of clusters of $Minpts$ localizations centered on point $i$. For $Minpts$ in the range 2–19, we calculated the Pearson's correlation coefficient between $\{cdist^i_{GR}\}$ and $\{cdist^i_{GG}\}$ to find out whether the spatial extent of green and red clusters is correlated.

1. Pertsinidis A, Zhang Y, Chu S (2010) Subnanometre single-molecule localization, registration and distance measurements. *Nature* 466(7306):647–651.
2. Heisenberg W (1950) *The Physical Principles of the Quantum Theory* (Dover, New York).
3. Thompson RE, Larson DR, Webb WW (2002) Precise nanometer localization analysis for individual fluorescent probes. *Biophys J* 82(5):2775–2783.
4. Mortensen KI, Churchman LS, Spudich JA, Flyvbjerg H (2010) Optimized localization analysis for single-molecule tracking and super-resolution microscopy. *Nat Methods* 7(5):377–381.
5. Yang X, Kaeser-Woo YJ, Pang ZP, Xu W, Südhof TC (2010) Complexin clamps asynchronous release by blocking a secondary Ca(2+) sensor via its accessory α helix. *Neuron* 68(5):907–920.
6. Pang ZP, Cao P, Xu W, Südhof TC (2010) Calmodulin controls synaptic strength via presynaptic activation of calmodulin kinase II. *J Neurosci* 30(11):4132–4142.
7. Deák F, et al. (2006) Rabphilin regulates SNARE-dependent re-priming of synaptic vesicles for fusion. *EMBO J* 25(12):2856–2866.
8. Arad N, Dyn N, Reisfeld D, Yeshurun Y (1994) Image warping by radial basis functions: Applications to facial expressions. *Comput Vis Graph Image Process* 56(2):161–172.
9. Rohr K, et al. (2001) Landmark-based elastic registration using approximating thin-plate splines. *IEEE Trans Med Imaging* 20(6):526–534.
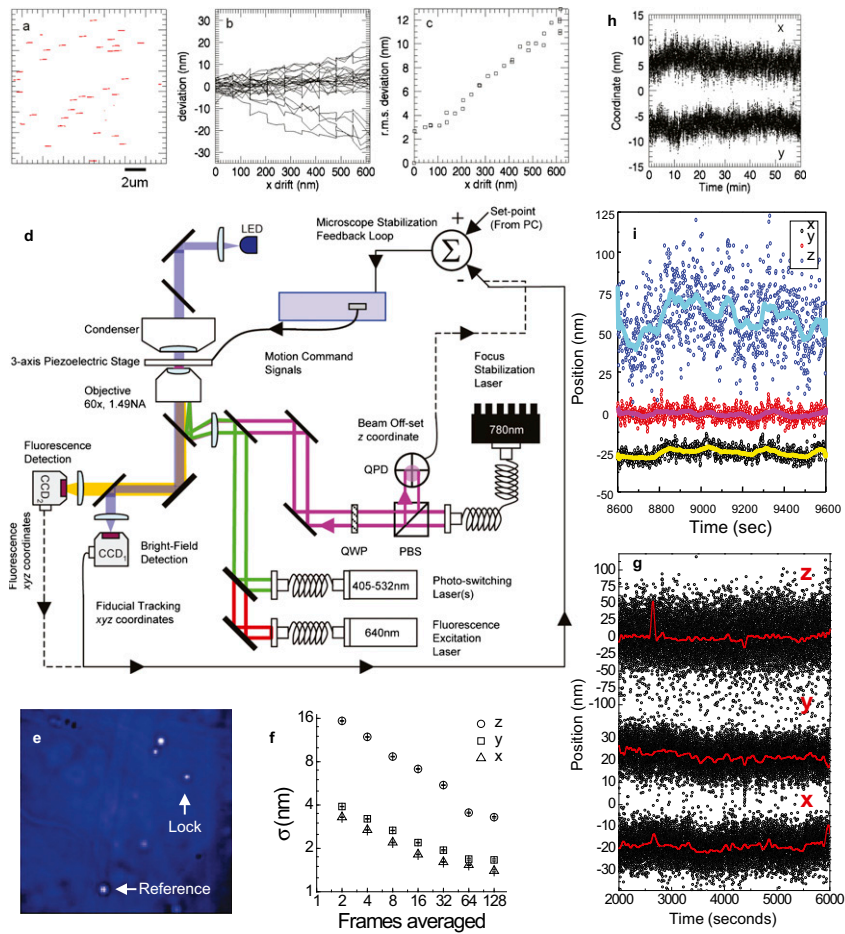
**Fig. S1.** Loss of position information due to drift and active microscope stabilization. (*A*) Trajectories of Cy5 molecules attached to the coverslip and imaged on CCD camera CCD2 in a 15 μm × 15 μm region of interest. To simulate "drift" in a controlled manner, the sample was translated using the piezoelectric 3D stage, in the *x* direction only and under closed-loop control (by tracking a 0.5-μm bead on CCD1) while the *y* and *z* coordinates are locked by the feedback system. (*B*) Residual deviations of the *x* coordinate of each Cy5 molecule after the mean drift has been subtracted, vs. amplitude of the drift. Similar results were obtained for the *y* coordinates. (*C*) rms deviations of the *x* positions of the Cy5 molecules after drift subtraction. Note that each Cy5 could be tracked to ~2.7-nm rms in each frame, whereas 500 nm drift increased the uncertainty in the position of each Cy5 to ~10 nm. (*D*) Experimental setup. The bright-field image was projected on a CCD camera (labeled CCD1) and fluorescence of the Cy3 and Cy5 dyes was imaged with a second CCD camera (labeled CCD2). For the laser-based focus-lock system, the combination of quarter-wave-plate (QWP) and polarizing beam splitter (PBS) creates an optical isolator that directs the back-reflected total internal reflection (TIR) beam on a position-sensitive detector (QPD). The position of the beam on the QPD encodes axial position of the coverslip surface. The real-time coordinates *xyz* of fiduciary marks (or *xy* from fiducials and *z* from the QPD) were fed to a digital servo-loop that controlled a three-axis piezoelectric stage to stabilize the microscope. (*E*) Bright-field image of neurons on CCD1, showing fiducials that were tracked by the feedback system. One fiducial is used to lock the 3D position of the microscope and the second serves as an out-of-loop reference. (*F*) The long-term rms stability of the microscope is ~1.5 nm in *xy* and <4.0 nm in *z*. (*G*) Trajectory of the *xyz* coordinates of the out-of-loop reference fiducial at 200-ms exposures. Red lines are 128-frame smoothed trajectories. (*H*) Relative registration between CCD cameras CCD1 and CCD2. We stabilized the microscope by tracking in real time a 0.5-μm bead, using CCD camera CCD1 and locking its *xyz* position with the piezoelectric stage. Simultaneously we imaged a separate 0.5-μm bead on CCD2 (fluorescence detection channel). We tracked this out-of-loop bead in CCD2 in *xy* to 1.1-nm rms at 144-ms exposures, while its position remained stable to <3 nm (peak-to-peak) over 1 h. (*I*) Alternative microscope stabilization scheme using fiducial tracking directly on CCD camera CCD2. Forty-nanometer fluorescent nanospheres (Transfluorospheres 488/645; Invitrogen) were attached to the coverslip surface and imaged on the same fluorescence channel as Cy5/Alexa 647. The apparent width of the nanosphere image *s*, as the focus was varied, was used to determine the axial position of the sample, with sensitivity d*s*/d*z* = 0.1 nm/nm. One nanosphere was used for stabilizing the stage and a second nanosphere served as an out-of-loop reference to monitor the performance of the feedback loop. The out-of-loop reference traces show $\sigma_x$, $\sigma_y$ = 3.5 nm and $\sigma_z$ = 17 nm 3D tracking at 1 Hz (open symbols) whereas the long-term stability is 1.5 nm in *xy* and 8.5 nm in *z* rms, respectively (solid lines, 64-frame average).

**Fig. S2.** Precision and photon-count histograms for Cy5, Alexa 647, and Atto532. (*A*) (*Top*) Cy5-DNA, (*Middle*) Alexa 647-PHD F-actin, and (*Bottom*) Alexa 647-antibody superresolution imaging. (*Left*) Histograms of localization precision $\sigma = \sqrt{\sigma_x \sigma_y}$; $\sigma$ was calculated according to Eq. **S1a**. *Insets* show cumulative distributions. (*Right*) Histograms of number of photons collected from each Cy5/Alexa 647 molecule in each on cycle. Red lines are linear semilog fits, indicating an exponential distribution $D(N) \sim \exp(-N/N_0)$. (*B*) Atto 532-labeled antibodies. *Inset* shows cumulative distribution. Red solid line: double-exponential fit. The mean number of collected photons for Atto 532 is 13,216 in this case.

**Fig. S3.** Resolution refinement based on photon counts. (*A*) Theoretical enhancement of FWHM resolution vs. cutoff ratio $\nu \equiv \frac{\sigma_0}{\sigma_{cutoff}}$ in the background-free case. See *SI Methods* for details. Starting at an initial FWHM($D$) = 2.828$\sigma_0$ ($\beta(0)$ = 2.828), the resolution is improving as a smaller $\sigma_{cutoff}$ is chosen (blue curve), and the ratio $\beta(\nu) \equiv FWHM(D)/\sigma_0$ drops with increasing $\nu$. For sufficiently small $\sigma_{cutoff}$ the resulting distribution will have a FWHM($D$) ~ 2.355$\sigma_{cutoff}$ (red curve, showing a plateau in the ratio). (*B*) Fraction $\alpha$ of localization data kept in the statistical refinement process vs. cutoff ratio $\nu$. As a progressively more stringent localization precision cutoff is enforced (increasing ratio $\nu \equiv \sigma_0/\sigma_{cutoff}$), the fraction of localization points that survives drops as $\exp(-\nu^2)$. (*C*) Theoretical enhancement of FWHM resolution vs. fraction $\alpha$ of localization data kept. The blue curve show the ratio of the FWHM resolution over $\sigma_0$, starting at $\beta$ (1) = 2.828 for the initial Lorentzian distribution. As a more stringent cutoff is enforced, the resolution improves ($\beta$ decreases) but also the number of points decreases. If only $\alpha$ ~ 10% of the localization data are kept, an improvement of approximately twofold can be expected ($\beta$ (0.1) ~ 1.4). For a practical limit of $\alpha$ ~ 1% the expected enhancement is ~3× ($\beta$ (0.01) ~ 0.9). In the asymptotic regime [red curve plateau $\gamma(\alpha \rightarrow 0)$ = 2.355], further improvement in the resolution is sub-logarithmic in $\alpha$, $\beta \propto \frac{2.355}{\sqrt{-\log(\alpha)}}$.

**Fig. S4.** Resolving individual antigens and epitope saturation/spatial sampling controls. (*A–C*) Resolving individual SNAP-25 antigens in close proximity. (*A*) Black dots are Alexa 647 localization points (Fig. 3C). Red circles indicate the locations of identified individual SNAP-25 antibodies. (Scale bar: 100 nm.) *B* and *C* show profiles of the density of the localization points across cuts indicated in *A*. Blue lines show fits to Gaussian peaks. The 13-nm FWHM of the clusters of localization points allows us to clearly resolve individual Alexa 647-labeled SNAP-25 antibodies at distances 30–50 nm. (*D*) Successive imaging of the same region verifies adequate spatial sampling. Syntaxin-1 Alexa 647-labeled primary antibody localizations are shown. Red symbols are the first 1,500 frames during the acquisition; black symbols are the last 1,500 frames. (Scale bar: 320 nm.) (*E–P*) Demonstration of saturation of SNAP-25 and syntaxin-1 epitopes and adequate spatial sampling. A first round of staining with Atto 532 syntaxin-1 primary antibody (*E* and *F*) was followed by a second round with Alexa 647 syntaxin-1 (*G*) or SNAP-25 (*H*) primary antibody. Similarly, Alexa 647-SNAP-25 (*K* and *L*) primary antibody was followed by Atto 532 SNAP-25 (*M*) or syntaxin-1 (*N*) primary antibody. Both syntaxin-1 and SNAP-25 epitopes can be saturated in the first round of staining, resulting in negligible signal from the second antibody (*G* and *M*). If epitopes are available, the second antibody gives robust signal (*H* and *N*). (*I, J, O,* and *P*) MAP-2 counterstaining using a rabbit polyclonal and Alexa 488 secondary antibody.

**Fig. S5.** Density-based clustering structure and correlation analysis for syntaxin-1 and SNAP-25 localizations. (*A*) Syntaxin-1 (red) and SNAP-25 (green) localizations. *Inset* illustrates the definitions of $cdist_{GR}$ and $cdist_{GG}$ for *Minpts* = 7. (*B*) Ordered plots (index calculated using the OPTICS algorithm) of the core distances $cdist_{GR}$ and $cdist_{GG}$ for the data points in *A* for cluster size *Minpts* = 10. (*C* and *D*) Pearson's correlation coefficient (*C*) for {$cdist^i_{GR}$, $cdist^i_{GG}$} and mean core distance (*D*) ($cdist^i_{GR} \times cdist^i_{GG}$)$^{0.5}$ for *Minpts* in the range 2–19. (*E*) Pair-distribution functions for syntaxin-1 Alexa 647 and SNAP-25 Atto 532 antibody localizations (Fig. 3*B*). The solid curves are exponential fitting to the data with decay lengths $\xi_{stx\text{-}stx}$ = 42 nm and $\xi_{SN25\text{-}SN25}$ = 48 nm for syntaxin-1 and SNAP-25, respectively. The decay to zero at $r < 15$ nm is due to the fact that overlapping antibodies at about the resolution limit are not resolved.

**Fig. S6.** Two-color nanometer colocalization calibration: (*A*) Nano-fabricated hole array. SEM image of an array with 1-μm spacing is shown. (Scale bar: 1 μm.) (*B*) Diameter of holes increases with e-beam dose. Two-color mapping calibration: (*C*) Nanohole array image. (*Upper*) Cy3 channel; (*Lower*) Cy5 channel. (Scale bar: 5.12 μm.) (*D*) Registration using a polynomial transformation. (Scale bar: 5.12 μm.) (*E*) Residuals of polynomial transformation. (Scale bar: 20 nm.) (*F*) Registration accuracy for Cy3-Cy5 DNA molecules using spline-interpolation of the nanohole array coordinate data. (*G*) Residuals of the Cy3-Cy5 DNA mapping over the whole field of view.
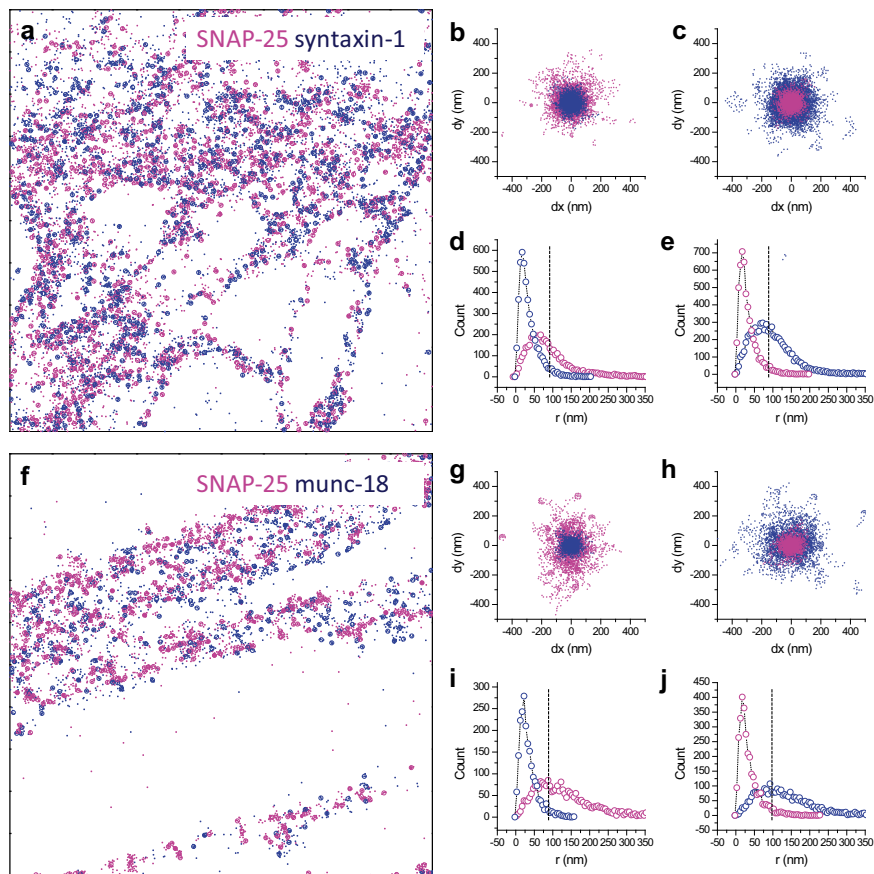
**Fig. S7.** Quantitative colocalization of SNAP-25, syntaxin-1, and Munc18-1. (*A* and *F*) Clusters of SNAP-25/syntaxin-1 (*A*) and SNAP-25/Munc18-1 (*F*) localizations were identified using the DBSCAN algorithm with *Minpts* = 3 and $\varepsilon_{SNAP-25/syntaxin-1}/\varepsilon_{syntaxin-1/SNAP-25}$ = 32.0 nm and $\varepsilon_{SNAP-25/Munc18-1}$ = 28.8 nm, $\varepsilon_{Munc18-1/SNAP-25}$ = 38.4 nm in *A* and *F*, respectively. About 67–75% of all of the molecules are assigned to clusters and the solid circles in each scatter plot represent the centroid of each identified cluster. (*B*, *C*, *H*, and *G*) The average profiles of syntaxin-1 (*B*), SNAP-25 (*C* and *H*), and Munc18-1 (*G*) clusters were obtained by centering each cluster at the origin (*x*, *y* = 0), by subtracting for each cluster {(*x*$_i$, *y*$_i$)} the mean coordinates (*x*$_i^c$, *y*$_i^c$). For each cluster centered at the origin the nearest cluster of the opposite species is identified and overlaid in the scatter plots. (*D*, *E*, *I*, and *J*) Corresponding radial distributions of the first species centered clusters and overlaid second species nearest-neighbor clusters. Ninety-five percent of all of the clustered molecules are contained within a radius indicated by the vertical dashed lines. The fraction of the second species' clustered molecules that are contained within the 95% radius quantifies the colocalization between the two molecules and is 62%, 49%, 34%, and 37% for (*D*) syntaxin-1/SNAP-25, (*E*) SNAP-25/syntaxin-1, (*I*) Munc18-1/SNAP-25, and (*J*) SNAP-25/Munc18-1, respectively.
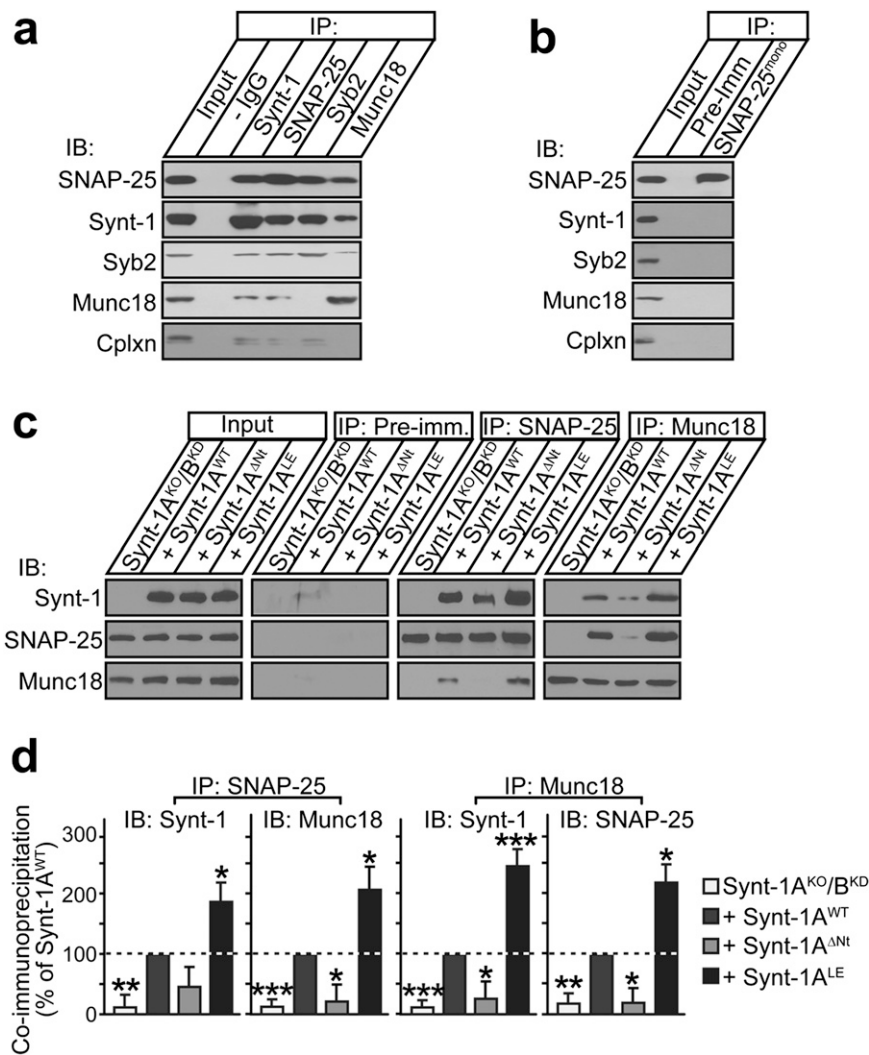
**Fig. S8.** Interaction of Munc18-1 and SNAP-25 via syntaxin-1. (*A*) Wild-type mouse brain lysate (P50) was subjected to immunoprecipitaton of SNAP-25, syntaxin-1 (Synt-1), synaptobrevin-2 (Syb-2), and Munc18-1 (Munc18), as well as a control immunoprecipitation without antibody (−IgG). To detect coimmunoprecipitated proteins, the immunoprecipitate samples and 5% of the input were separated by SDS/PAGE and immunoblotted (IB) with indicated antibodies (Cplxn, complexin-1,2). (*B*) Wild-type mouse brain lysates were used for immunoprecipitation as in *A*, using an antibody specific to monomeric SNAP-25 (SNAP-25$^{mono}$) as well as control immunoprecipitation using preimmune serum (Pre-Imm). Coimmunoprecipitated proteins were detected by immunoblotting as indicated. (*C*) Lysates were prepared from syntaxin-1A KO mouse cortical cultures infected with syntaxin-1B KD lentiviruses (Synt-1A$^{KO}$/B$^{KD}$) without or with rescue expression of the wild type (+Synt-1A$^{WT}$), N-terminal deletion (+Synt-1A$^{\Delta Nt}$), or LE mutant (+Synt-1A$^{LE}$) variants of Syntaxin-1A. Lysates were used for immunoprecipitation of SNAP-25 and Munc18, as well as control immunoprecipitation with preimmune serum (Pre-Imm). Input and immunoprecipitates were separated as in *A* and immunoblotted using Synt-1, SNAP-25, and Munc18 antibodies (*Upper*). Extent of coimmunoprecipitation was quantitated using $^{125}$I-labeled secondary antibody and phosphorimager analysis (*Lower*). (*D*) Level of coimmunoprecipitated protein was first normalized to immunoprecipitated protein and then to expression level in the input and is shown as percentage of wild-type rescue. Data shown are means ± SEMs; n = 3 cultures; *P < 0.05, **P < 0.01, ***P < 0.001, using Student's *t* test.

**Table S1. Numerical parameters**

| Sample | $N_{photons}$ | $N_{frames}$ | $(b^2)$* | $(b_{eff}^2)$† | $s$, pixels | $\sigma_0$, nm‡ | $\sigma_0$, nm§ | Expected FWHM, nm¶ | Actual FWHM, nm‖ |
|---|---|---|---|---|---|---|---|---|---|
| dsDNA | 8,450 | 1.98 | 63.6 | 126.0 | 2.18 | 2.5 | 2.9 | 8.2 | 9 |
| F-actin | 3,110 | 1.37 | 36.2 | 49.4 | 2.16 | 4.2 | 4.8 | 13.6 | 17 |
| Antibody | 5,680 | 1.41 | 69.2 | 96.4 | 2.25 | 3.4 | 3.85 | 10.9 | 13 |

*$b^2$ in units of (photons$^2$/pixel).
†$b_{eff}^2 = \langle N_{frames} b^2 \rangle$.
‡Calculated from Eq. **S1a**.
§Calculated from Eq. **S1b**.
¶Expected FWHM is equal to $2\sqrt{2}\sigma_0 \approx 2.828\sigma_0$.
‖Peak fits of the data in Figs. 1 *A* and *C* and 2*B*.